Master's thesis
Your Field

Formation of cores by merging supermassive black holes

Joonas Suortti

August 9, 2019

Tutor: prof. Smith

Censors: prof. Smith
doc. Smythe

UNIVERSITY OF HELSINKI
Department of Something

PL 42 (Kuvitteellinen katu 1)
00014 Helsingin yliopisto

"Bachelor's degrees make pretty good placemats if you get them laminated."

—Jeph Jacques

HELSINGIN YLIOPISTO — HELSINGFORS UNIVERSITET — UNIVERSITY OF HELSINKI

Tiedekunta — Fakultet — Faculty		Laitos — Institution — Department
Faculty of Whatever		Department of Something
Tekijä — Författare — Author		
Joonas Suortti		
Työn nimi — Arbetets titel — Title		
Formation of cores by merging supermassive black holes		
Oppiaine — Läroämne — Subject		
Your Field		
Työn laji — Arbetets art — Level	Aika — Datum — Month and year	Sivumäärä — Sidoantal — Number of pages
Master's thesis	August 9, 2019	0 pages

Tiivistelmä — Referat — Abstract

Abstract goes here.

Avainsanat — Nyckelord — Keywords

Your keywords here

Säilytyspaikka — Förvaringsställe — Where deposited

Muita tietoja — övriga uppgifter — Additional information

Contents

1. Introduction

2. Theory

3. KETJU

Description of basic functionality: what KETJU does, why it's created, basic description of the multiple integration region system.

3.1 AR-CHAIN

Chain forming, force calculations, integration

3.2 GADGET-3

Softening, tree-codes, calculations

3.3 Combined Functionality

How the AR-CHAIN and GADGET-3 integrators work together: time-step problem, tidal-perturbations, particles moving from one region to another, chain macro-particle

3.3.1 Particle Types

3.4 Black Hole Trajectories

Since we are trying to determine if merging SMBH binaries form cores in merger remnants, we must make sure that the progenitors' central black holes actually merge in our simulations. This is done by looking at the "Run" simulations, as they contain the locations of the black holes from multiple time steps, and as the "Snapshots" still show both of the SMBHs.

Plotting the positions of the black holes from "Run 3" in coordinates centred on the binary's centre-of-mass during the initial time step gives us figure 3.1. Even by eye, one can clearly see that the orbit of the black hole with a smaller mass becomes smaller and smaller as the binary moves further away from its initial position. While this doesn't explicitly tell us that the black holes merge into each other, it does indicate the existence of a hardening process in the binary. Similar figures to figure 3.1 from all four "Runs" can be found in the appendix (figure B.1).

The most likely obstacle for the complete merging of the binary black holes is the so-called final-parsec problem; where, due to the lack of stellar material that can be ejected during the three-body scattering phase, the hardening of the binary stops when the separation between the two black holes is $\sim$ 1pc. This is assumed to happen since, not only is the binary constantly ejecting the finite amount of stars inside the loss-cone (defined in section 2), but the loss cone itself is becoming smaller due to the contracting binary orbit.

Figure 3.2 shows the time evolution of both the semi-major axis and the eccentricity of the binary orbits from all of the simulation runs. Interestingly enough the semi-major axes of all of the binaries go far below single parsec scales, meaning that the final-parsec problem doesn't seem to play a part in the simulations. This implies that, there exists some loss-cone refill mechanism which allows the binary

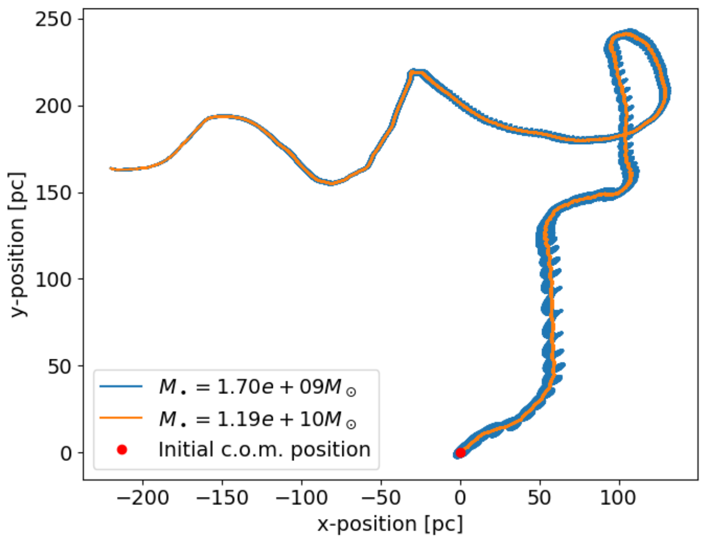

Figure 3.1: The trajectories of the black holes during "Run 3". The coordinates are centred on the initial location of the centre-of-mass of the binary black hole. The orange and blue lines show the paths taken by the smaller and larger black holes respectively. Both paths show clear spiral patterns which become smaller and smaller as the simulation proceeds. The paths end at the location where the black holes merge, i.e. where the distance between them is $\lesssim 100R_s$ (R_s is the Schwarzschild radius).

to eject more stellar material than what initially exists inside the loss cone.

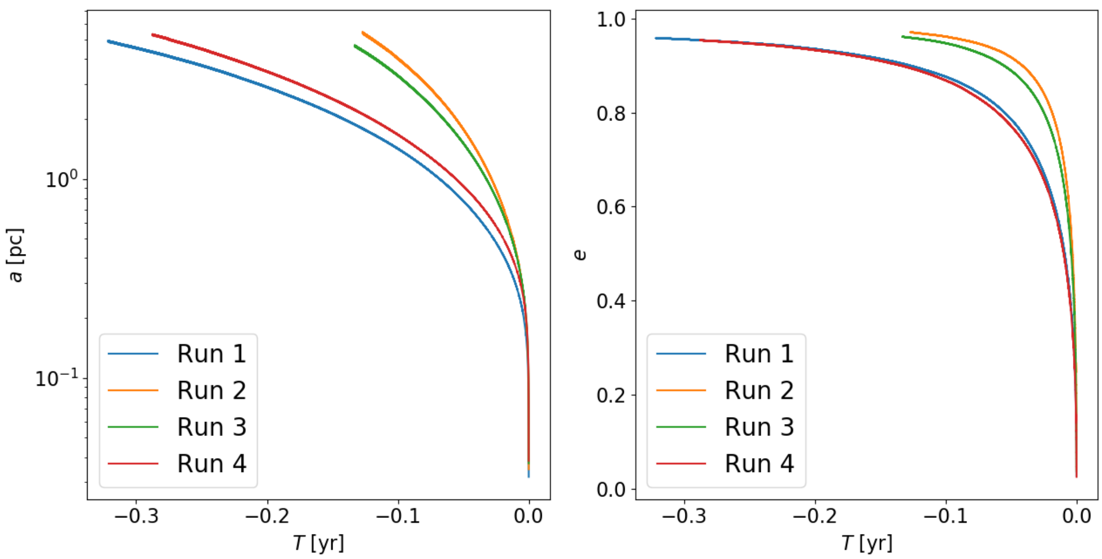

Figure 3.2: The semi-major axes (left) and eccentricities (right) of the black hole systems in the simulations "Runs 1"-"Run-4" as a function of time. The zero position on the x-axis corresponds to the point in simulation time, where the black hole merging event occurs.

4. Merger Simulations Using KETJU

In this chapter I study the formation of cored galaxies through galaxy mergers by analysing results from KETJU simulations by Rantala et al. (2018). The merger progenitor galaxies in these simulations contain central supermassive black holes. During the merger event the SMBHs form a hard binary, a likely source for the observed cores, as it can eject stars from the galactic centre through complex three-body interactions. Here I determine if there is a connection between the binary SMBH and the existence of a core deficient in light, and if the simulated KETJU results agree with observations.

4.1 Simulation Details

The simulations done by Rantala et al. (2018) include seven different mergers of two identical galaxies. The merger progenitor galaxies used in the different simulations (named BH-0 - BH-6) are comprised of stellar and dark matter particles, with the different particle types having identical masses. The progenitors are gas free (i.e. the simulations describe so-called "dry" mergers), and most of them contain an SMBH at their centre.

The central SMBHs in the progenitors are simply modelled as point masses located at the origin of the galaxy's internal coordinate system; while the stellar and dark matter particles are distributed according to the spherically symmetric Dehnen density-potential model (Dehnen, 1993):

$$\rho(r) = \frac{(3-\gamma)M}{4\pi} \frac{a}{r^{\gamma}(r+a)^{4-\gamma}}, \tag{4.1}$$

$$\phi(r) = \frac{GM}{a} \times \begin{cases} -\frac{1}{2-\gamma}\left[1-\left(\frac{r}{r+a}\right)^{2-\gamma}\right] & \gamma \neq 2 \\ \ln \frac{r}{r+a} & \gamma = 2 \end{cases}, \tag{4.2}$$

where M is the total mass, a is a scaling radius, and γ is the central slope of the profile. For stellar particles $\gamma = 3/2$, while for the dark matter particles $\gamma = 1$.

Using the Dehnen density-potential model, the positions of the different particles are determined through its cumulative mass profile:

$$M(r) = 4\pi \int_0^r \rho(r) r^2 \, dr = M \left(\frac{r}{r+a}\right)^{3-\gamma}, \tag{4.3}$$

where $\rho(r)$ is the density profile from equation 4.1. Once the positions of the particles are known, their velocities can then be determined using the Eddington's formula (Binney and Tremaine, 2008), which gives the following distribution function for the different particles in the position-velocity phase-space:

$$f_i(\varepsilon) = \frac{1}{\sqrt{8}\pi^2} \int_{\Phi_T=0}^{\Phi_T=\varepsilon} \frac{d^2\rho_i}{d\Phi_T^2} \frac{d\Phi_T}{\sqrt{\varepsilon - \Phi_T}}, \tag{4.4}$$

where ρ_i is the density profile from equation 4.1 for the particle in question, Φ_T is the total gravitational potential, and ε is the relative energy:

$$\varepsilon = -\Phi_T + \Phi_0 - \frac{1}{2}v^2, \tag{4.5}$$

where v is the velocity of the particle, and Φ_0 is a chosen zero point for the potential. This zero point is usually chosen so that, $f > 0$ for $\varepsilon > 0$, and $f = 0$ for $\varepsilon \leq 0$. In the case of the analysed simulations $\Phi_0 = 0$, as the modelled galaxies are isolated and extend to infinity.

The physical parameters needed for generating the progenitor galaxies using equations 4.3 and 4.4 are given in table 4.1 under "Common physical properties", and, as name implies, are identical across all of the progenitors used in the simulations. While the uses for the number of stellar and dark matter particles, and the stellar and dark matter masses, are self-explanatory; the effective radius R_e and dark matter fraction inside the half-mass radius $f_{\mathrm{DM}}(r_{1/2})$ are used for determining the scaling radius a with the equations:

$$a_\star = r_{1/2}(2^{1/(3-\gamma)} - 1); \quad r_{1/2} \approx 4/3 R_e, \tag{4.6}$$

and

$$a_{\mathrm{DM}} \approx \frac{4}{3}\left[\sqrt{\frac{2M_{\mathrm{DM}}}{M_\star}\left(\frac{1}{f_{\mathrm{DM}}(r_{1/2})} - 1\right)} - 1\right] R_e, \tag{4.7}$$

, for the stellar and dark matter particle profiles respectively. The values for these common properties are motivated by observations and dynamical simulations of NGC 1600 (Rantala et al., 2018), an early-type cored galaxy with a large core radius and a central supermassive black hole with a mass of $\sim 1.7 \times 10^{10} M_\odot$ (Thomas et al., 2016).

Table 4.1 also shows the masses of the central SMBHs in each of the seven progenitor galaxies. The mass of the central SMBH is the only physical property that changes from one progenitor to another. Six of the progenitor galaxies (BH-1 - BH-6) contain central supermassive black holes, with the SMBH masses varying from $8.5 \times 10^8 M_\odot$ to $8.5 \times 10^9 M_\odot$, where a merged binary of the largest SMBHs is equivalent in mass to the central SMBH in NGC 1600. The seventh progenitor (BH-0) does not contain an SMBH in its centre, and is included simply for the sake of comparison.

The simulations themselves comprise of seven mergers of two identical progenitor galaxies from table 4.1. The galaxies are merged on a nearly parabolic orbit with an initial separation of d = 30kpc since, according to Rantala et al. (2018),

Common physical properties						
$M_\star$	R_e	M_{DM}	$f_{\mathrm{DM}}(r_{1/2})$	$N_\star$	N_{DM}	
4.15	7	7.5	0.25	4.15×10^6	1.0×10^7	
$M_\bullet$						
BH-0	BH-1	BH-2	BH-3	BH-4	BH-5	BH-6
-	0.85	1.7	3.4	5.1	6.8	7.5

Table 4.1: Physical properties of the different progenitors used in the simulations by Rantala et al. (2018).

$M_\star$: Stellar mass [$\times 10^{11} M_\odot$]

R_e: Effective radius [kpc]

M_{DM}: Dark matter halo mass [$\times 10^{13} M_\odot$]

$f_{\mathrm{DM}}(r_{1/2})$: The fraction of dark matter mass from the total mass inside the effective radius

$N_\star$: Number of stellar particles

N_{DM}: Number of dark matter particles

$M_\bullet$: Central SMBH Mass [$\times 10^{9} M_\odot$]

this kind of orbit makes the approach of the galaxies swift, and causes the stellar cusps to merge before $t \sim 300$Myr.

The simulation data that I will be analysing, comes in the form of a snapshot of the merger remnant. These snapshots are taken at the simulation time of $\sim$ 2Gyr, at which point the progenitor galaxies have merged into a single merger remnant galaxy which contains an SMBH binary in its centre. The snapshots contain the positions, velocities and masses of every particle; be they stellar particles, dark matter particles or black holes.

4.2 Core Size Measurements

In order to check if a galaxy is cored or not, I calculate its surface brightness profile and check if the galaxy contains surface brightness deficiencies near its centre.

The surface brightness profiles are calculated from the merger remnant snapshots by: changing the coordinate system to centre-of-mass coordinates, projecting the stellar particles onto a 2D plane, and calculating the mass inside logarithmically spaced radial bins to get a radial surface mass density profile. The aforementioned calculations are repeated 100 times from random viewing angles, which results in 100 slightly different density profile projections. These profiles are then averaged azimuthally, which results in a smooth surface mass density profile, that can then be turned into a surface brightness profile by assuming some mass-to-light ratio for the stellar particles (Rantala et al., 2018). However, as the only properties that the stellar particles have in the snapshot are: their position and velocity at a singular point in time, as well as a mass that is identical to the mass of every other stellar particle; it is not possible to make valid, physically accurate, assumptions on their specific mass-to-light ratios. For this reason, a constant mass-to-light ratio of $M/L = 4$ is used, which is equivalent to the ratio derived from dynamical modelling of NGC 1600 by Thomas et al. (2016).

Figure 4.1 shows example surface brightness profiles for every simulated merger remnant. Looking at the different curves, one can already see that the presence of central SMBHs in the merger progenitors causes some kind of brightness deficiency near the centre of the merger remnant. Not only that, the larger the mass of the central black holes, the larger the surface brightness deficiencies are.

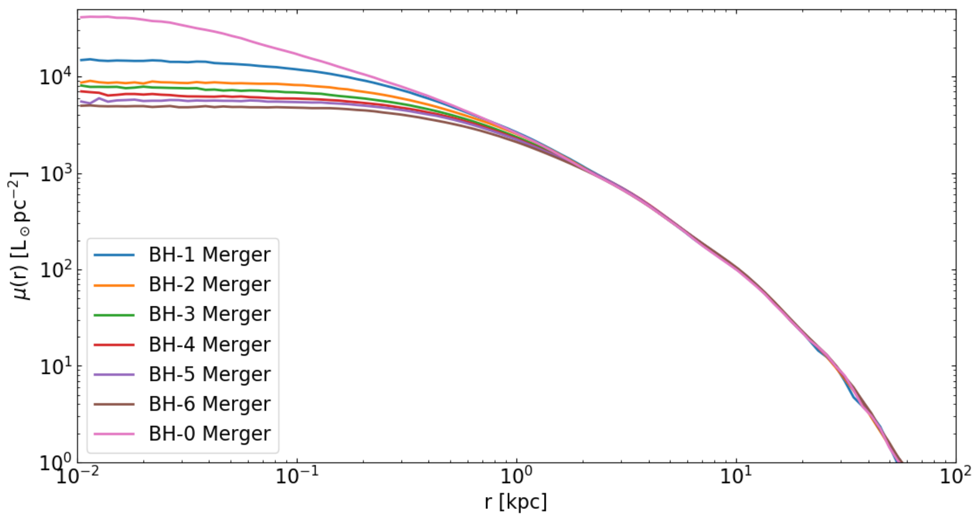

Figure 4.1: Surface brightness profiles from every simulated merger remnant. These were calculated by dividing the simulated galaxy remnants into 100 radial logarithmic bins, and averaging the surface brightness inside the bins through 100 random viewing angles. The luminosity of the particles was estimated by assuming a mass-to-light ratio of $M/L = 4$.

The deficiencies found in the surface brightness profiles reveal the presence of cores; however, determining the precise sizes of the cores require us to find the exact locations where the deviations from the expected power-law profile start. This can be done by fitting the derived brightness profile with a model that is a combination of two power laws: a shallow inner power-law, and a steeper outer power-law. The radius at which the power laws shift, i.e. the break radius r_b, is defined as the radius of the core.

There are two commonly used options for modelling the surface brightness profiles. The first one is the core-Sérsic profile (Graham et al., 2003a), which can be expressed using the following equation:

$$\mu(r) = \mu' \left[1 + \left(\frac{r_b}{r}\right)^{\alpha}\right]^{\gamma/\alpha} \exp\left\{-b_n \left[\left(r^{\alpha} + r_b^{\alpha}\right)/r_e^{\alpha}\right]^{1/(\alpha n)}\right\}, \tag{4.8}$$

where r_b is the break radius, γ is the logarithmic slope of the inner power-law, α controls the sharpness of the transition between the two power-laws, r_e and n are the effective half-mass radius and the Sérsic index of the outer power-law, and the normalization factor μ' is defined by:

$$\mu' = \mu_b 2^{-\gamma/\alpha} \exp\left[b_n \left(2^{(1/\alpha)} r_b/r_e\right)^{1/n}\right], \tag{4.9}$$

where μ_b is the surface brightness at the break radius.

The second option is to use the so called Nuker profile (Lauer et al., 1995):

$$\mu(r) = 2^{(\beta-\gamma)/\alpha} \mu_b \left(\frac{r_b}{r}\right)^{\gamma} \left[1 + \left(\frac{r}{r_b}\right)^{\alpha}\right]^{(\gamma-\beta)/\alpha}, \tag{4.10}$$

where r_b is once again the break radius, μ_b is the surface brightness at the break radius, β and γ are the logarithmic slopes of the power-laws inside and outside of the break radius respectively, and α is the sharpness of the transition between the two slopes.

We calculate the core radii of the merger remnants by using the "Levenberg-Marquardt" fitting algorithm to fit both the core-Sérsic model and the Nuker model to the remnant's surface brightness profile. Figure 4.2 shows a comparison of the resulting fits for the BH-3 merger (refer to table 4.1), while figures B.2 and B.3, located in the appendix, show the fits for every remnant that contains SMBH binaries. The values of the best-fit parameters are written on the figures.

The root-mean-square of the fits' residuals are comparable to those seen in profile fits of observed surface brightness profiles: $\Delta \approx 0.02$ mag arcsec^{-2} (Dullo and Graham, 2012). However, while the RMS of the residuals show that the fits describe the surface brightness profiles well, they do contain some parts that show systematically larger residuals than others.

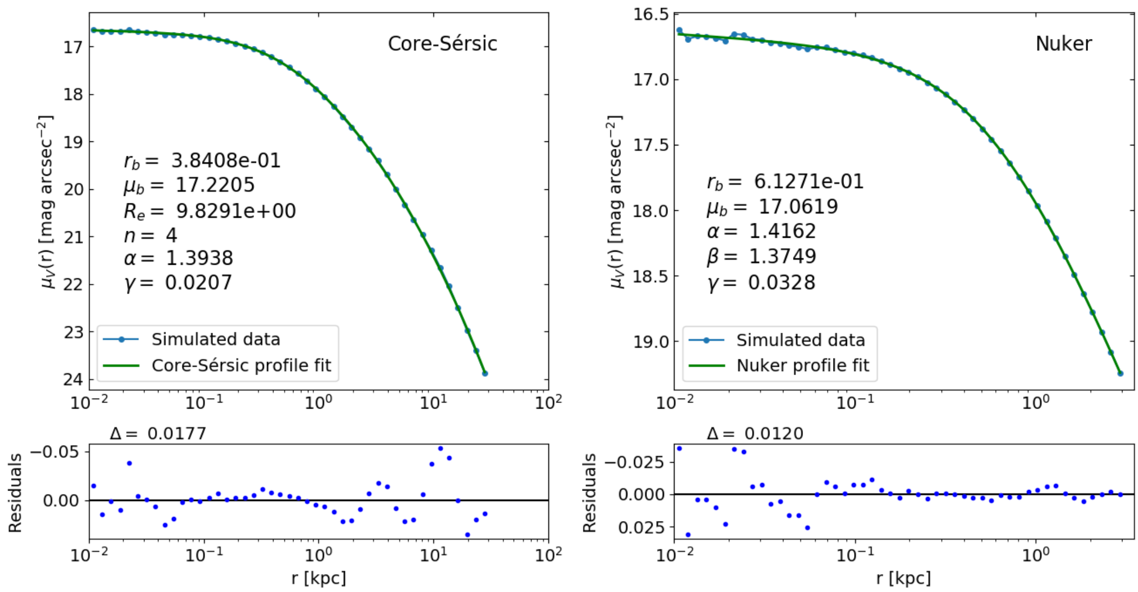

Figure 4.2: Core-Sérsic and Nuker profile fits of surface brightness profiles calculated from Snapshot 3 (left and top-right figures). The best fit parameters are written on the figures and are in the same units as the axes (i.e. r_b and R_e in kilo-parsecs, and μ_b in V-band magnitudes per arc-second squared). The relative residuals of the fits are plotted under their respective figures. The delta describes the root-mean-square of the residuals.

Most of the fits have large residual scatter near the centre of the merger remnant. This is especially noticeable in the Nuker fits, as their fitting range is concentrated at the galactic centre. However, this central residual scatter is most likely not indicative of any kind of physical merger remnant core structure; but a result of the logarithmic spacing of the bins in the surface brightness profiles. The bins near the centre are inherently smaller than the outer ones; which causes larger variation in the binned masses, and thus luminosities, when calculating the projected surface brightness profiles from different angles. This results in a final average profile, where the central regions contain small random variations in luminosity, which naturally causes the residuals of the fits to be scattered in a random way. These residuals are also larger, as the fitted profiles do not take these random variations into account.

Interestingly, all of the core-Sérsic fits show a peak in the size of the residuals at around $\sim$ 10kpc. Once again, this residual property is probably not an actual physical property found in merger remnants, but the result of using mostly identical initial conditions. However, the fact that it appears in the surface brightness profile from every simulation indicates that; even though the masses of the SMBHs in the merger progenitors have a large effect on the central regions of the merger remnant, the outer regions are left unaffected for the most part. This clearly implies that the simulations vary significantly from each other only due to the formation of the central SMBH binary, as the concentration of the variations in the centre of the merger remnant can be explained by the limited range of the sphere-of-influence of the binary.

Figures B.2 and B.3 show that the core radius estimate depends quite strongly on the used model. However, which model is better for estimating the size of the core is still a matter of debate (Lauer et al., 2007b; Dullo and Graham, 2012). While the RMS of the relative residuals seems to be consistently (although just marginally) smaller for the Nuker model, when compared to the RMS for the core-Sérsic model (compare figures B.2 and B.3), one also has to take into account that in the Nuker model the best-fit value for r_b is strongly dependent on the fitting range (Graham et al., 2003b). Furthermore, as stated by Rantala et al. (2018), in order to get sensible values for all of the model parameters (e.g. $\alpha \lesssim 1$ might even prevent the model from describing the profile as a combination of two power-laws), the fitting range of the Nuker model has to be narrowed down closer to the galactic centre. This, when combined with the parameters' high dependence of the fitting range, brings into question the sensibility of using the Nuker model for core radius estimation.

One could also estimate the size of the core without model fitting by calculating the so-called "cusp radius" r_γ, i.e. the distance from the galactic centre at which the logarithmic slope of the surface brightness profile $\gamma' = -1/2$ (Carollo et al., 1997; Lauer et al., 2007a). Because the cusp radius r_γ also provides an estimate for the location where the inner power-law of the profile changes into the outer power-law, it equates to the core radius.

We calculate r_γ for all of the merger remnants with SMBH binaries (BH-1 - BH-6 mergers) by calculating the gradient of the surface brightness profiles, and then using a "Nelder-Mead" minimization algorithm to find the radius, at which the gradient gets the value $-1/2$.

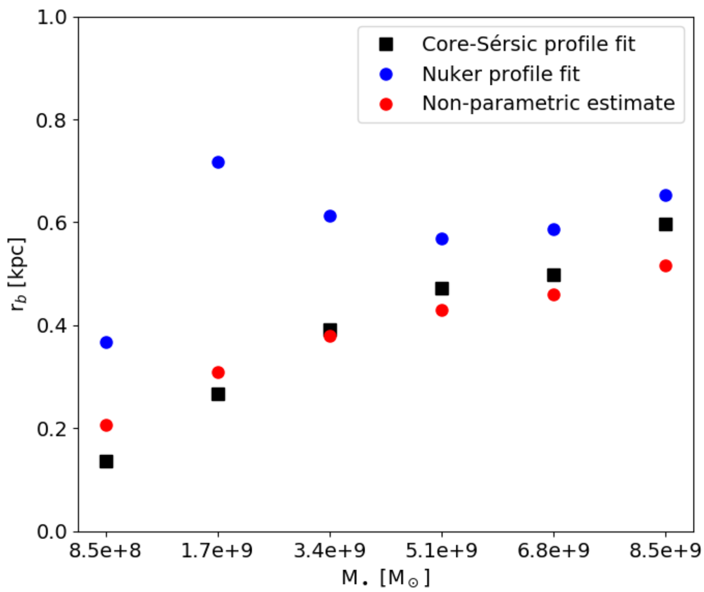

Figure 4.3: Comparison of the core radii of the merger remnants, gained through three different methods: Core-Sérsic profile fitting (black squares), Nuker profile fitting (blue circles) and finding the "cusp radius" (red circles). The x-axis shows the masses of the central SMBHs of the merger progenitors.

Figure 4.3 compares the core radius estimates from each of the three methods for every simulated merger remnant. The break radii from the Nuker fits are consistently larger than the other core radius estimates. They also have, in general, the largest deviations from the other core radius estimates. Nevertheless, when not accounting for a few of the Nuker break radii, a clear trend of the size of the core growing with the merger progenitors' central SMBH masses can be seen.

The size of the core being dependent on the mass of the central SMBH binary is clear evidence towards the cores being formed through a scouring process by the binary black holes. Binaries with larger masses have larger gravitational spheres-of-influence, which naturally leads to the ejection of stellar particles that orbit farther away from the galactic centre.

This positive correlation between the core size and the binary mass has also been identified in independent measurements of the break radius and the central SMBH mass in cored galaxies (e.g. de Ruiter et al., 2005; Lauer et al., 2007a; Thomas et al., 2016). The fact that this effect can be seen, not only in the simulations but also observations, greatly increases the credibility of the SMBH binary being the source of the core.

The clear trend of the surface brightness deficit becoming larger with the SMBH mass, as seen in figure 4.1, can also be explained trough scouring by an SMBH binary. (Bender et al., 1994)BinneyTremaine explain that only stars with the angular momentum:

$$L \lesssim [G(M_1 + M_2)a]^{1/2}, \tag{4.11}$$

where M_1 and M_2 are the masses of the binary black holes, interact strongly enough with the binary to be ejected from the system (i.e. are inside the loss-cone). As the above equation shows, the upper limit of this condition grows alongside the binary mass. Since this causes more of the orbiting stellar particles to be located in the strong interaction range, the larger SMBH binary mass naturally result in the ejection of a larger number of stellar particles, which then results in the growth of the central surface brightness deficit.

4.3 Velocity Anisotropy

Another way to find out that a galaxy has formed a core through core scouring by binary black holes, is to study its velocity anisotropy profile defined in Binney and Tremaine (2008) as:

$$\beta(r) = 1 - \frac{\sigma_\theta^2 - \sigma_\phi^2}{2\sigma_r^2} = 1 - \frac{\sigma_t^2}{\sigma_r^2}, \tag{4.12}$$

where σ_θ, σ_ϕ and σ_r are velocity dispersions in the spherical coordinates, and $\sigma_t = \sqrt{(\sigma_\theta^2 + \sigma_\phi^2)/2}$ is the tangential velocity dispersion. This β parameter describes the ratio of tangential velocity dispersion in the stellar system to the radial velocity dispersion, and as such, gives information about the nature of the stellar orbits around the black hole binary. A negative value for β shows an abundance of tangential orbits, where as a positive β an abundance of radial orbits.

Figure 4.4 shows β-profiles calculated from all of the final merger remnant snapshots using equation 4.12. According to the profiles, the outer areas of the remnants are dominated by radial orbits, while the majority of orbits near the centre are tangential.

As the progenitors used in the simulations contained β-profiles which had a constant value of $\beta = 0$, an area with negative β in the merger remnant would imply that the stars on radial orbits have been ejected from the system. It has been shown that hardening black hole binaries can eject stars on highly radial orbits from the galactic core, which results in the central region becoming dominated by mostly tangential orbits (and thus a negative β). The ejected stars can, in turn, cause the outer orbits to become more radial (Quinlan and Hernquist, 1997; Milosavljević and Merritt, 2001; Thomas et al., 2014).

This could certainly be the reason behind the shapes of the β-profiles seen in figure 4.4. The figure clearly shows that the presence of an SMBH binary has an effect on the profiles' shape; as not only does the slope of the profile steepen as the mass of the SMBH binary grows; but the only merger with a profile, completely

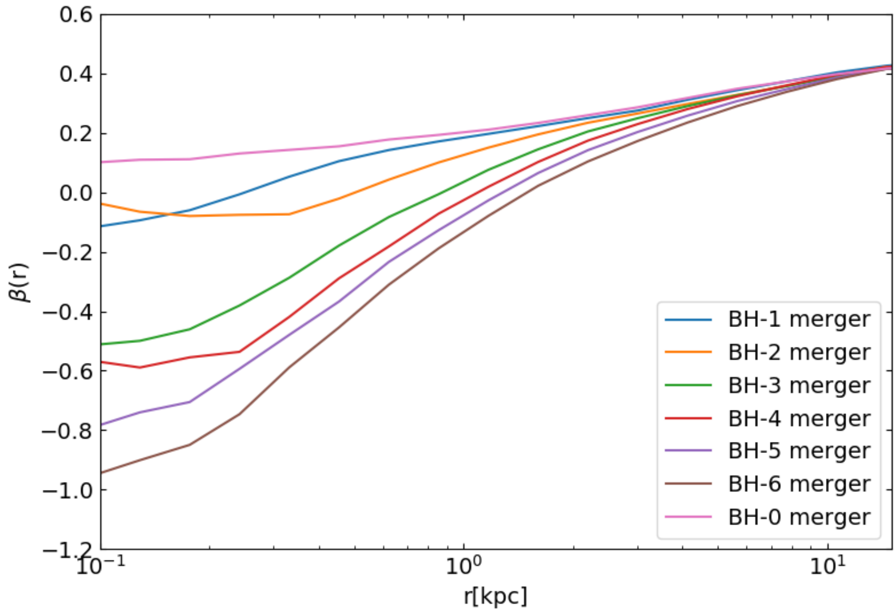

Figure 4.4: Velocity anisotropy (beta) profiles for every simulated merger remnant.

dominated by the radial velocity dispersion, is the one without a central binary.

The properties seen in the profiles also make sense in the context of ejection of stellar particles by hardening black hole binaries. The larger the mass of the SMBH biary is, the larger its gravitational sphere-of-influence, which results in more of the radially orbiting stellar particles being ejected.

Figure 4.5 shows, both the β-profile from NGC 1600 and the profiles from the simulated merger remnants, relative to the core radius of the respective galaxy. Even by eye, it can be seen that the β-profiles from both simulations and NGC 1600 are similar to each other (not counting the profile for the BH-2 merger). However, looking closely at the values on the axes of the plots, the observed profile of NGC 1600 seems to be somewhat steeper than any of the simulated ones.

According to Rantala et al. (2018) it is likely that, the higher steepness of the profile seen in NGC 1600 is due the simulations only comprising a single generation of completely isotropic ($\beta = 0$) mergers. Most observed cored galaxies, including

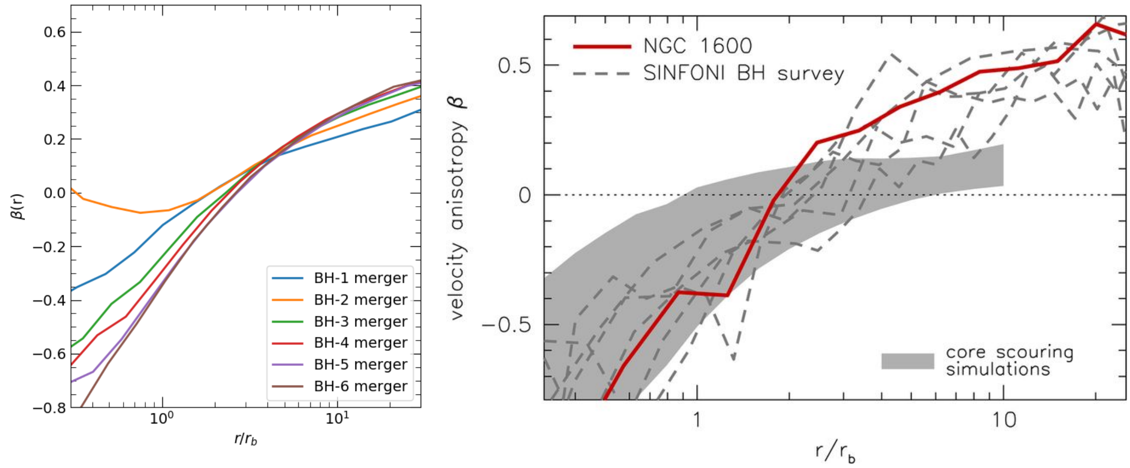

(a) Simulated merger remnants **(b)** NGC 1600

Figure 4.5: (a): β-profiles of the simulated merger remnants as a function of distance from the centre, relative to the break radius. (b): β-profile of NGC 1600, alongside profiles of galaxies from the SINFONI black hole survey (references), and the range of anisotropies found in N-body simulations of the core scouring mechanism (Thomas et al., 2016).

NGC 1600, are most likely the result of multiple generations of mergers. Every subsequent merger event causes the β-profile of the merger remnant to steepen even further, which is caused by the progenitors already containing a tangentially-biased centre and radially-biased outer regions as a result of the previous merger events.

It is also possible, that the reason why the outer region of the NGC 1600 β-profile is more radially dominated than any of the outer parts in the simulated merger remnants is due to the lack of minor-mergers in the simulations (Rantala et al., 2018). These minor-mergers would disrupt some of the outer tangential orbits, making them more radial. Furthermore, they would not contribute to the destruction of radial orbits near the centre of the galaxy, as the smaller progenitor galaxy would not contain a central SMBH.

4.4 Line-of-Sight Kinematics

4.4.1 2D Kinematic Maps

In order to make sure that the KETJU simulations produce results equivalent to observations, I analyse the line-of-sight (LOS) kinematics of the simulated merger remnants. The analysis is focused on four different LOS velocity distribution properties: the average LOS velocity V_{avg}, the velocity dispersion σ, and the h_3 and h_4 parameters which correspond to the skewness and the kurtosis of the distribution respectively. The distribution from which these properties are calculated is defined as the following modified Gaussian function (van der Marel and Franx, 1993; Bender et al., 1994):

$$f(v) = I_0 e^{-\gamma^2/2}(1 + h_3 H_3(y) + h_4 H_4(y)), \tag{4.13}$$

where I_0 is a normalization constant, γ is the central slope of the particle density profile, $y = (v - V_{\mathrm{avg}})/\sigma$, and H_3 and H_4 are the third and fourth order Hermite polynomials respectively:

$$H_3(y) = \left(2\sqrt{2}y^3 - 3\sqrt{2}y\right)/\sqrt{6}, \tag{4.14}$$

$$H_4(y) = \left(4y^4 - 12y^2 + 3\right)/\sqrt{24}. \tag{4.15}$$

In order to calculate the above properties, I first define the "line-of-sight" as the intermediate axis of the merger remnants, and orient the remnant accordingly using the inertia tensor. Next, a 2D line-of-sight projection of the remnant is divided into "spaxels" (or simply bins) using the voronoi tessellation algorithm (Cappellari and Copin, 2003). The shape and size of the spaxels are determined so that each one contains the same signal-to-noise ratio, which in our simulated case is defined as the number of stellar particles. The LOS-velocities inside the spaxels are then made into a histogram, into which the modified Gaussian function described in equation 4.13 is fitted. This gives the values of the LOS-velocity distribution parameters:

V_{avg}, σ, h_3 and h_4 for the spaxel in question. Finally, the values of the spaxels can be plotted, resulting in 2D voronoi binned maps of all of the four parameters.

Figure 4.6 shows the voronoi binned 2D maps of the four LOS velocity distribution parameters for the simulated BH-0 merger and the BH-6 merger, as well as for two observed galaxies NGC 3414 and NGC 4111. The contours, which are added to help visualise the shape of the galaxy, denote the merger remnants' flux isophotes, and have a spacing of one magnitude. Similar maps for every merger remnant can be seen in figures B.4 and B.5 in the appendix.

The IFU maps in figures B.4 and B.5 show that the average LOS velocities of the simulated merger remnants are far from isotropic, with most of the remnants containing central binary SMBHs showcasing counter-rotating central regions or "kinematically decoupled cores" (KDC). Some of the simulated remnants (BH-4 - BH-6 mergers) even contain another counter rotating structure inside the KDC. These features, alongside the relatively low average LOS-velocities, are found in galaxies called "slow rotators" (Emsellem et al., 2007). Slow rotator galaxies are early type galaxies which are assumed to have been formed through gas-poor "dry" mergers (Emsellem et al., 2007; Cappellari et al., 2007); processes not unlike the ones simulated in our simulations. As such, the merger remnants being slow rotators is a somewhat expected result. However, it also implies that the KETJU simulations do produce physically accurate results.

Figures B.4 and B.5 also contain IFU-maps of the velocity dispersion in the merger remnants, and show that the velocity dispersion is dependent on the mass of the central SMBH binary. The map for the merger remnant without black holes, shows a σ-distribution where the largest values of the velocity dispersion are located in two peaks along the minor axis of the galaxy. However, in the simulations with progenitors that contained SMBHs; the σ-distribution contains only one peak at the centre of the galaxy, the strength of which correlates positively to the mass

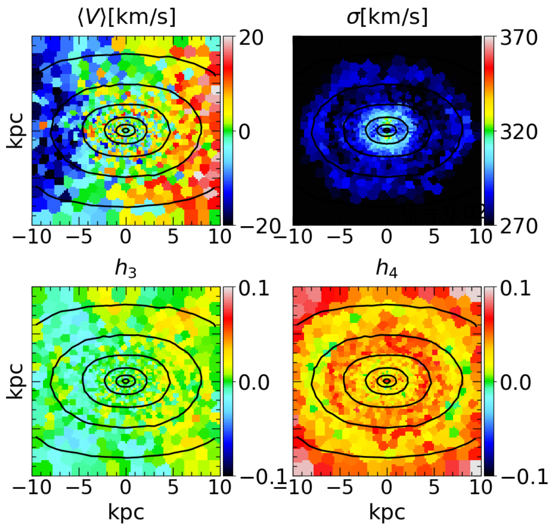

(a) BH-1 merger remnant

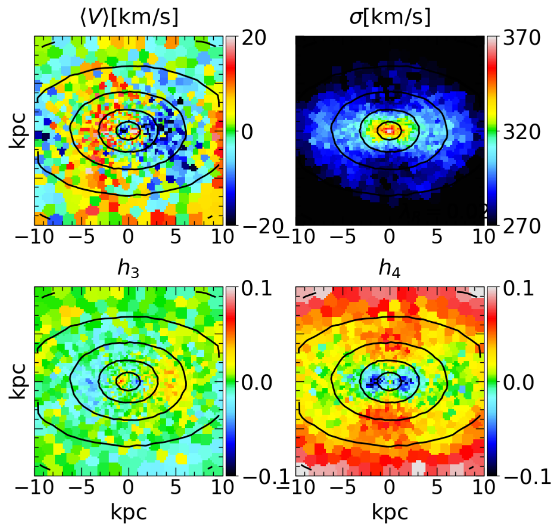

(b) BH-6 merger remnant

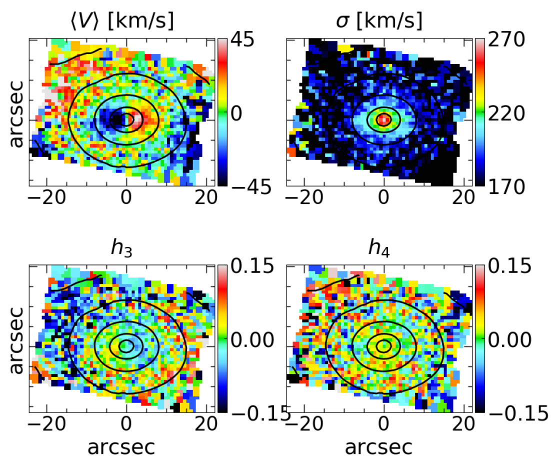

(c) NGC 3414

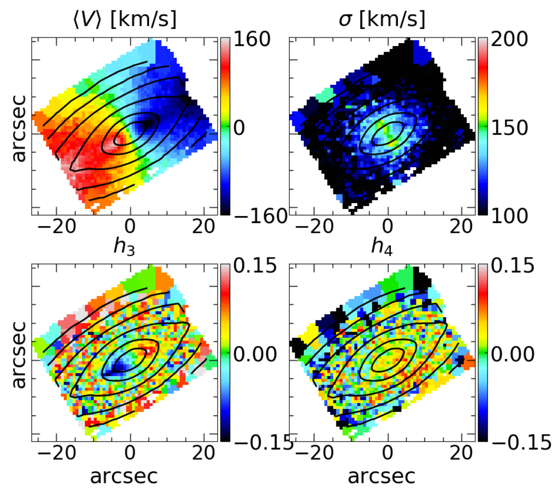

(d) NGC 4111

Figure 4.6: IFU-maps of average LOS-velocities, velocity dispersion, h_3 parameters and h_4 parameters from two simulated merger remnants and two observed galaxies. The four maps in figure (a) are from the BH-0 merger, and the four in figure (b) are the BH-6 merger. Figures (c) and (d) show IFU-maps of known slow (NGC 3414) and fast rotator (NGC 4111) galaxies from the ATLAS^{3D} survey (Emsellem et al., 2004; Cappellari et al., 2011; Krajnović et al., 2011).

of the central SMBH binary. Furthermore, instead of the minor axis, the largest velocity dispersion values are located along the major axis of the galaxy, with the area of largest velocity dispersion growing alongside the SMBH binary mass. The differences between the simulations without a central binary and the simulation with the most massive binary are demonstrated in Figure 4.6.

The positive correlation between the mass of the central SMBH (or in the case of the simulations: central SMBH binary) and the velocity dispersion of its host galaxy has been observed in a multitude of galaxies with central SMBHs, cored of otherwise (Ferrarese and Merritt, 2000). The fact that this correlation can also be identified in the simulated merger remnants provides further evidence towards the KETJU simulation results being physically accurate.

Apart from the BH-0 merger remnant, the h_3-parameter values in the IFU-maps of the simulated merger remnants show an anti-correlation with the average LOS-velocity. Indeed, Krajnović et al. (2011) have found that, while the anti-correlation between the LOS velocities and the h_3-parameter is mostly found in fast rotators, some galaxies with counter-rotating cores (CRC) also exhibit this behaviour. This anti-correlation can be seen in NGC 3414 from figure 4.6. Once again, the KETJU results are similar to the observations.

The h_4-parameter roughly corresponds to the velocity anisotropy parameter β, where a negative value of h_4 identifies areas with a large tangential velocity dispersion, and a positive identifies areas of more radial velocity dispersion (Gerhard, 1993; Gerhard et al., 1998; Thomas et al., 2007). Comparing the β-profiles from figure 4.4 with the h_4 IFU-maps from figures B.4 and B.5, this certainly seems to be the case. For the merger remnants with central SMBH binaries, both the β and the h_4 values are largely positive in the outer regions of the galaxy, while being negative closer to their centres. The h_4 map of the BH-0 merger is then positive all around, exactly like its β-profile. The h_4 maps of NGC 3414 nor NGC 4111 (figure 4.6) do not contain any specific structures and seem to be completely isotropic. As the negative areas in the IFU maps of the simulated merger remnants are likely caused by core scouring, and as neither of the observed galaxies are cored galaxies (Lauer et al., 2007b); they most likely have not experienced such a process, making the lack of clear structures understandable.

4.4.2 The λ_R-parameter

Further analysis on the kinematics of the simulated merger remnants can be done by looking at the λ_R parameter, which describes the angular momentum of a galaxy (Emsellem et al., 2007). More importantly, the parameter allows us to differentiate between the aforementioned slowly rotating galaxies and so-called fast rotators (see figure 4.6) (Emsellem et al., 2007). The parameter itself is defined in a general form as:

$$\lambda_R \equiv \frac{\langle R|V|\rangle}{\langle R\sqrt{V^2+\sigma^2}\rangle}, \tag{4.16}$$

where R is the projected distance from the galactic centre, V is velocity, σ is the velocity dispersion and $\langle\ \rangle$ denote that the nominator and denominator in the equation are luminosity weighted means. However, as most of the observational kinematic analysis of galaxies is done through binned 2D spectroscopy, and as the IFU-maps made from our simulations are produced the same way as the observed ones, we will be using the following version of the equation:

$$\lambda_R = \frac{\sum_{i=1}^{N_p} F_i R_i |V_i|}{\sum_{i=1}^{N_p} F_i R_i \sqrt{V_i^2+\sigma_i^2}}, \tag{4.17}$$

where F_i, R_i, V_i and σ_i are the flux, projected distance from the galaxy centre, velocity and velocity dispersion of the ith bin, and N_p is the number of bins. In the case of our simulations, the N_p bins used are of course the voronoi bins described earlier in this section.

Determining whether a galaxy is either a fast or a slow rotator using λ_R, is done by comparing the value that the parameter gets at the galaxy's effective radius, to some pre-defined threshold. The originally used threshold is: $\lambda_{Re} < 0.1$, where λ_{Re} is the aforementioned λ_R at the effective radius, and where galaxies fulfilling the condition are classified as slow rotators (Emsellem et al., 2007). A revision of the threshold by Emsellem et al. (2011) takes the ellipticity (ϵ) of the galaxy into account, and defines slow rotators as having $\lambda_{R_e} < 0.31\sqrt{\epsilon}$, which accounts for the increased anisotropy in the kinematics of flatter galaxies. An even further refinement of the threshold has been proposed by Cappellari (2016), where slow rotator galaxies are determined using the following two criteria: $\lambda_{R_e} < 0.08 + \epsilon/4$ and $\epsilon < 0.4$. The former criterion of the threshold reduces the risk of misidentifying very round non-regular slow rotators as fast rotators, while the latter makes sure that only sufficiently round galaxies are classified as slow rotators (Cappellari (2016) argues that "genuine" disk-less slow rotators are all rounder than $\epsilon = 0.4$).

Since two of the three aforementioned slow rotator thresholds require us to know the ellipticity of the galaxy, we calculate the simulated merger remnants' ellipticities before analysing their rotation. The ellipticity calculations are done using a method described in Zemp et al. (2011), which uses the shape tensor:

$$\mathbf{S} = \frac{\int_V \rho(\mathbf{r})\omega(\mathbf{r})\mathbf{r}\mathbf{r}^T \, dV}{\int_V \rho\mathbf{r} \, dV}, \tag{4.18}$$

where $\mathbf{r}$ is position from the galactic centre, $\rho(\mathbf{r})$ is the mass density, V is the volume of an enclosed ellipsoid with the elliptical radius r_{ell}, and where the weighting function $\omega(\mathbf{r}) = 1$. The eigenvalues of the shape tensor correspond to $a^2/3$, $b^2/3$ and $c^2/3$; where a, b and c are the semi-principal axes; and which can be used to calculate the ellipticity as $\epsilon = 1 - b/a$.

However, simply calculating the shape tensor and getting the correct eigenvalues is not possible, as the elliptical radius r_{ell} is defined, in part, by using the axis ratios a/b and a/c:

$$r_{\mathrm{ell}} = \sqrt{x_{\mathrm{ell}}^2 + \frac{y_{\mathrm{ell}}^2}{(b/a)^2} + \frac{z_{\mathrm{ell}}^2}{(c/a)^2}}. \tag{4.19}$$

This means that we have to turn the calculation into an iterative process by starting with $b/a = c/a = 1$ for the initial value of r_{ell}, and calculating new shape tensor eigenvalues using previously gained axis ratios until the values of the ratios start to converge.

We calculate λ_{Re} and ϵ_e, i.e. the ellipticity at the effective radius (the ellipticity is calculated using $r_{\mathrm{ell}} = R_e$, and a convergence criterion of a difference smaller than 10^{-3} between consequent axis ratios), for every merger simulation snapshot and plot them against each other. We also plot the previously mentioned slow rotator thresholds, as well as observations from the ATLAS$^{3\mathrm{D}}$-survey (Cappellari et al., 2011), in the same figure. The resulting plot can be seen in figure 4.7.

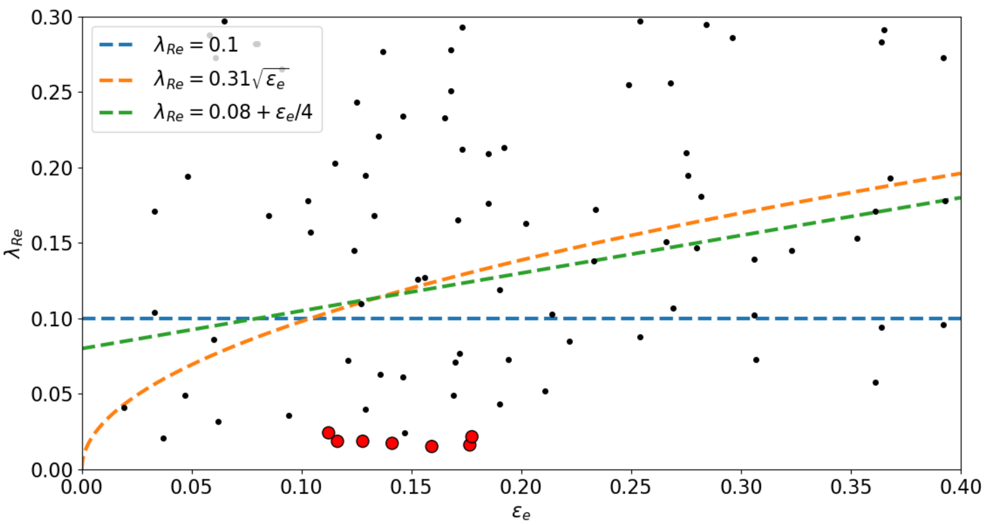

Figure 4.7: The values of the λ_{Re}-parameter of galaxies, plotted against their ellipticity at the effective radius. The red dots correspond to the simulated merger remnants, where as the black dots correspond to galaxies observed in the ATLAS$^{3\mathrm{D}}$-survey (Cappellari et al., 2011; Emsellem et al., 2011). The dashed lines display different slow rotator thresholds as a function of ellipticity (Emsellem et al., 2007, 2011; Cappellari, 2016).

Regardless of the threshold used for differentiating between slow and fast rotators, figure 4.7 shows us that, all of the simulated merger remnants are clearly classified as slow rotators. This agrees well with the kinematic anisotropies seen in the IFU maps, which also implied a slow rotator classification for the remnants.

4.5 Comparison to NGC 1600

As the physical properties of the merger progenitors are modelled after NGC 1600, it is interesting to see how the results from the simulations compare with actual observations of the galaxy. I am mainly comparing the observations to the BH-6 merger remnant, as the mass of the SMBH binary in the simulation is equivalent to the assumed mass of the central SMBH in NGC 1600 ($M_\bullet = 1.7 \times 10^{10} M_\odot$) (Thomas et al., 2016).

Figure 4.8 compares the core-Sérsic profile fits of the surface brightness profiles from BH-1 and BH-6 mergers to the profile fits from the observed core galaxies NGC 4472 and NGC 1600 respectively. Not only do the shapes of the profile fits follow each other closely in both cases, the best-fit parameters are also closely related (table A.1).

An even further comparison between some of the properties of the two galaxies can be seen in table 4.2. Most importantly the table shows that even their kinematic properties are alike, or in the very least, of the same order of magnitude. Furthermore, much like the merger remnants seen in the snapshots, by looking at its λ_e parameter and ellipticity at the effective radius, NGC 1600 can easily be identified as a slow rotator.

Being able to reproduce, not only the photometric qualities, but also the kinematic properties, of an observed galaxy is quite impressive. This clearly indicates that the KETJU code is able to simulate galaxy mergers in a physically accurate manner, and simulated process, i.e. core scouring by a binary SMBH during a galaxy

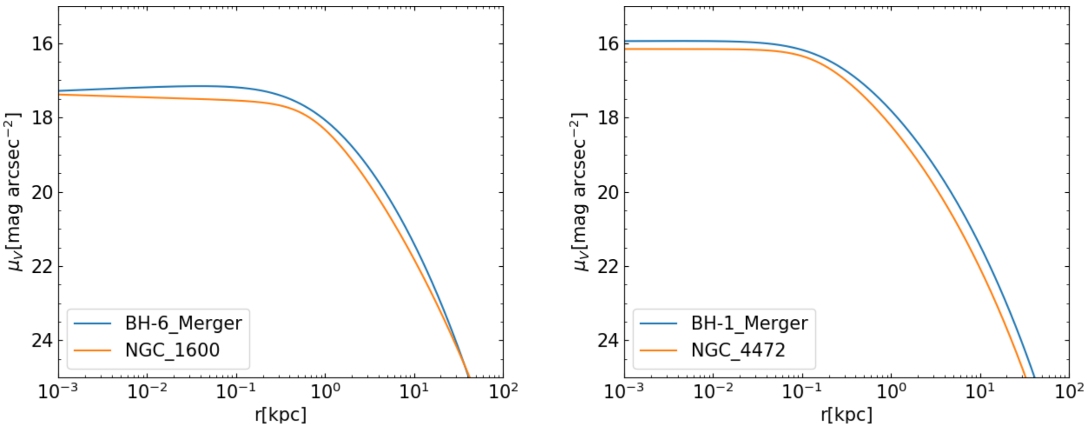

Figure 4.8: Comparison between core-Sérsic profile fits from observed galaxies and simulated merger remnants. The figure on the left compares the profile of the BH-6 merger remnant (the merger remnant whose progenitors containing the largest central SMBH massess) to NGC 1600; while the figure on the right compares the profiles of the BH-1 merger remnant (the remnant with progenitors that had the smallest SMBH masses) and NGC 4472. The parameters for plotting the core-Sérsic profile of NGC 1600 were taken from Thomas et al. (2016), with the units being changed to the above, by assuming $V - R = 0.5$ (the same assumption being done in Lauer et al. (2007b)), and by using the distance $D = 64$Mpc (Thomas et al., 2016) to define the relation between arc seconds and parsecs. The parameters for the profile of NGC 4472 were from Dullo and Graham (2012) and Lauer et al. (2007b). The best-fit parameters can be found from the appendix in table A.1

Galaxy	$M_\star$	$M_\bullet$	R_e	μ_e	n	$V_{\rm LOS}$	σ_e	λ_e	ϵ_e
	$[\times 10^{11} M_\odot]$	$[\times 10^{10} M_\odot]$	[kpc]	[mag/arcsec^2]		[km/s]	[km/s]		
(1)	(2)	(3)	(4)	(5)	(6)	(7)	(8)	(9)	(10)
BH-6 merger	8.3	1.7	8.914	17.7	4	5.84	311	0.0215	0.14
NGC 1600	8.3	1.7	~ 16	~ 22.8	5.83	3.4	293	0.026	0.32

Table 4.2: Comparison between the physical properties of the simulated merger remnant BH-6 merger and the galaxy NGC 1600. The properties described in the columns are explained below, with the sources for the properties of NGC 1600 being written inside the brackets.

(1) Name of the galaxy.

(2) Total stellar mass (Thomas et al., 2016).

(3) For BH-6 merger: central SMBH binary mass. For NGC 1600: central SMBH mass (Thomas et al., 2016).

(4) Effective radius (Thomas et al., 2016). For NGC 1600, the effective radius is changed from arc seconds to kpc by assuming that it is located at the distance of $D = 64$ Mpc (Thomas et al., 2016).

(5) Surface brightness at the effective radius. Calculated from the best fit core-Sérsic profile parameters given in Thomas et al. (2016).

(6) Sérsic index from the best fitting core-Sérsic profile fit (Thomas et al., 2016).

(7) Mean line-of-sight velocity inside the effective radius (Bender et al., 1994).

(8) Velocity dispersion inside the effective radius (Veale et al., 2017). For BH-6 merger, the given velocity dispersion is calculated from a Voronoi binned image as the mean of the velocity dispersion values of the bins located inside the effective radius.

(9) Spin parameter at the effective radius (Veale et al., 2018).

(10) For BH-6 merger: ellipticity of the galaxy at the effective radius; and for NGC 1600: luminosity weighted ellipticity (Goullaud et al., 2018).

merger, is most likely the driving mechanism behind core formation.

5. Conclusions

A. Tables

	BH-1 merger	NGC 4472	BH-6 merger	NGC 1600
r_b [kpc]	0.137	0.129	0.597	0.667
μ_b [mag arcsec^{-2}]	16.29	16.44	17.70	18.00
R_e [kpc]	9.717	8.709	8.914	1.604
n	4	4.3	4	5.83
α	1.44	2	1.16	2.09
γ	0.00	0.00	-0.04	0.03

Table A.1: Best fit parameters of the core-Sérsic profile fit seen in figure 4.8.

B. Figures

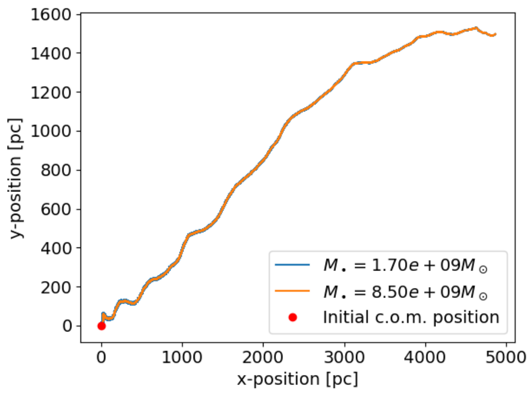

(a) Run 1

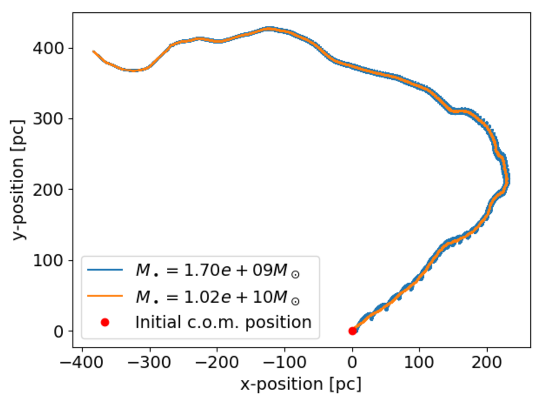

(b) Run 2

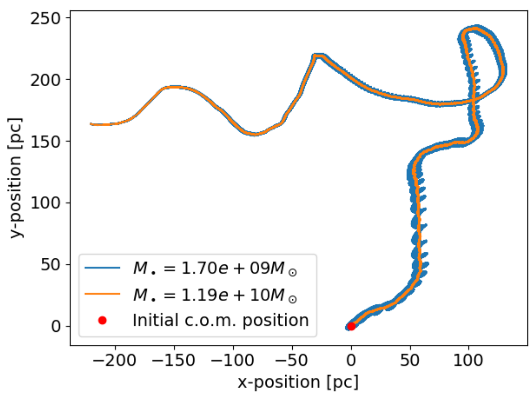

(c) Run 3

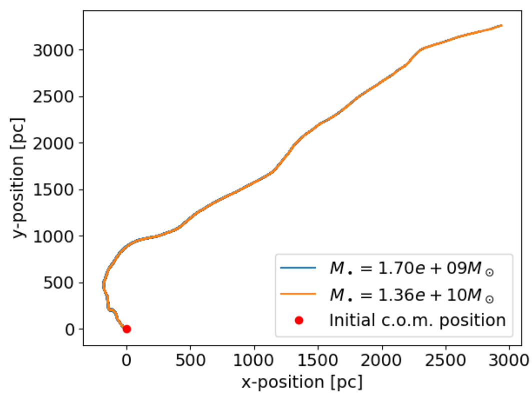

(d) Run 4

Figure B.1: The trajectories of the black holes from simulation runs by Mannerkoski et al. (2019). The coordinates are centred on the initial location of the centre-of-mass of the black hole system. The orange and blue lines show the paths taken by the smaller and larger black holes respectively during the simulation.

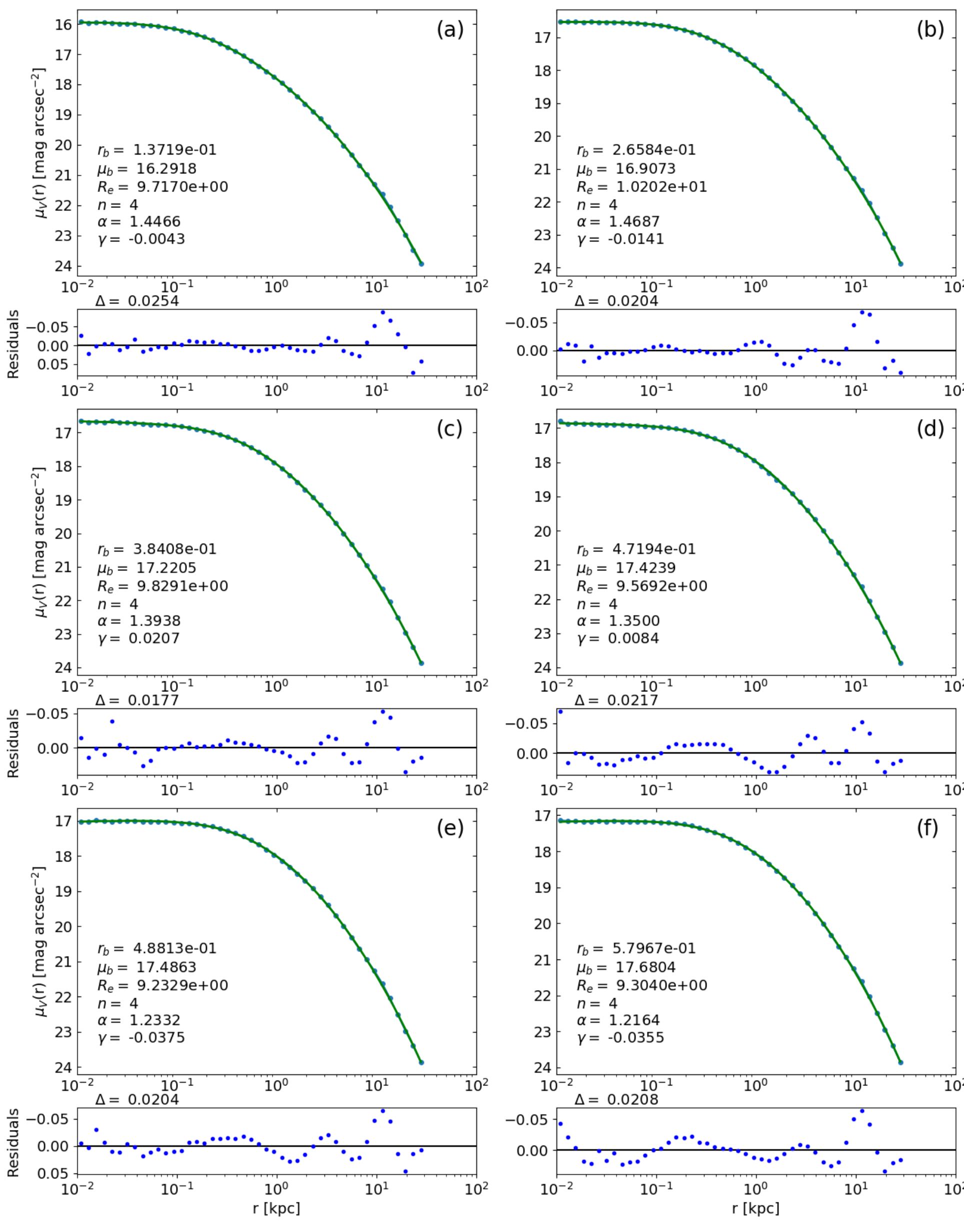

Figure B.2: Core-Sérsic profile fits of the surface brightness data calculated from all of the individual simulated merger remnants with progenitors containing central supermassive black holes. The letters (a)-(f) denote the different snapshots ((a): BH-1 merger, (b): BH-2 merger, (c): BH-3 merger, (d): BH-4 merger, (e): BH-5 merger, (f): BH-6 merger).

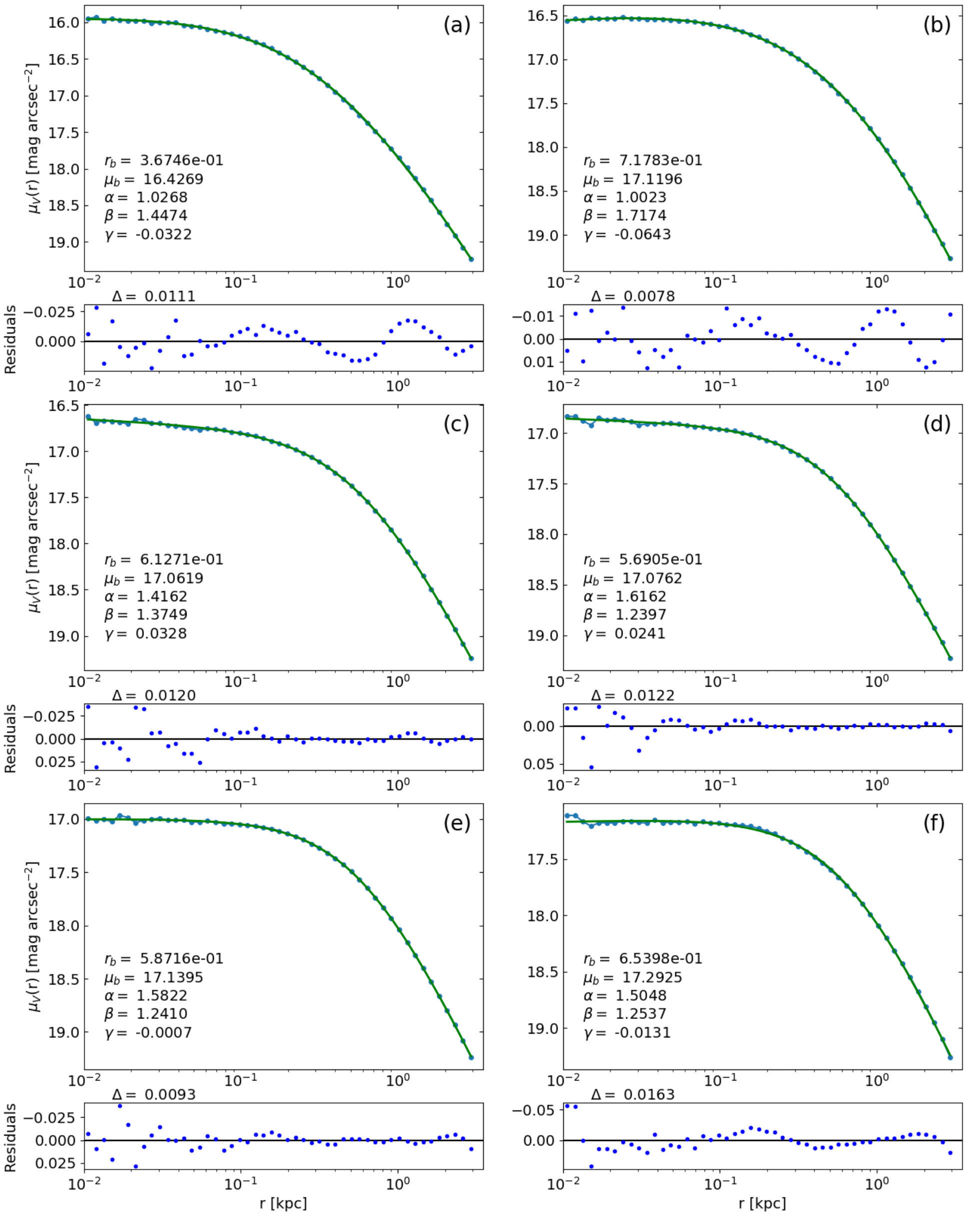

Figure B.3: Nuker profile fits of the surface brightness data calculated from all of the individual simulated merger remnants with progenitors containing central supermassive black holes. The letters (a)-(f) denote the different merger remnants ((a): BH-1 merger, (b): BH-2 merger, (c): BH-3 merger, (d): BH-4 merger, (e): BH-5 merger, (f): BH-6 merger).

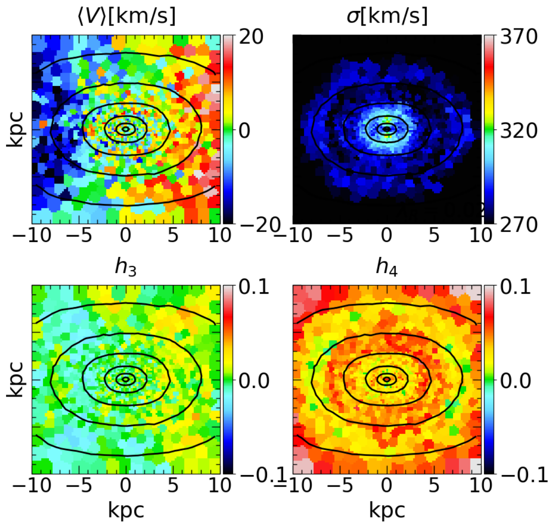

(a) BH-0 merger

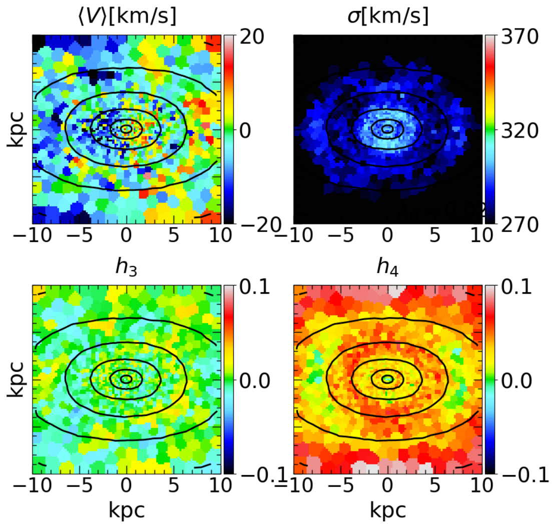

(b) BH-1 merger

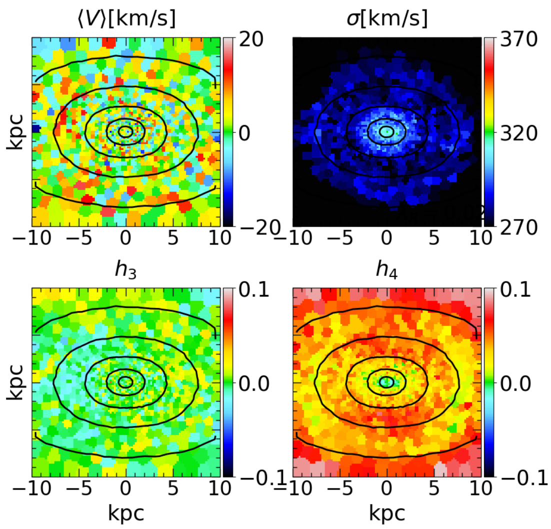

(c) BH-2 merger

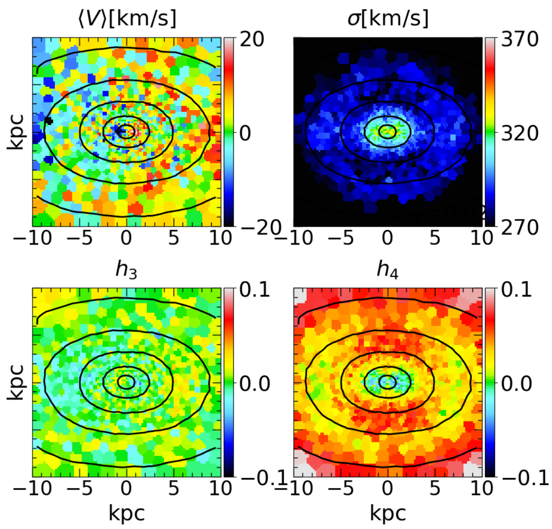

(d) BH-3 merger

Figure B.4: IFU-maps of average LOS-velocities, velocity dispersion, h_3 parameters and h_4 parameters from four simulated merger remnants: Snapshot-0, Snapshot-1, Snapshot-2 and Snapshot-3.

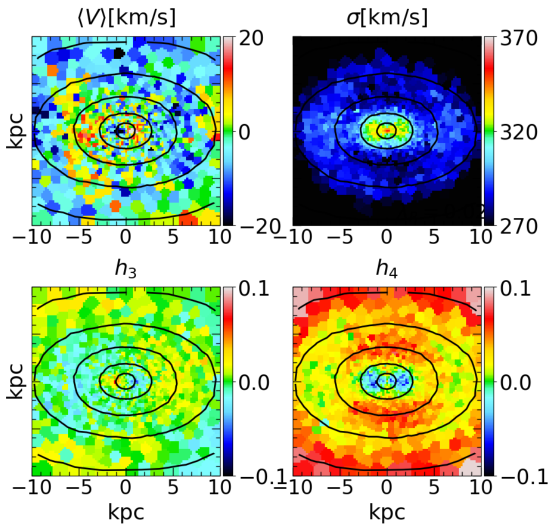

(a) BH-4 merger

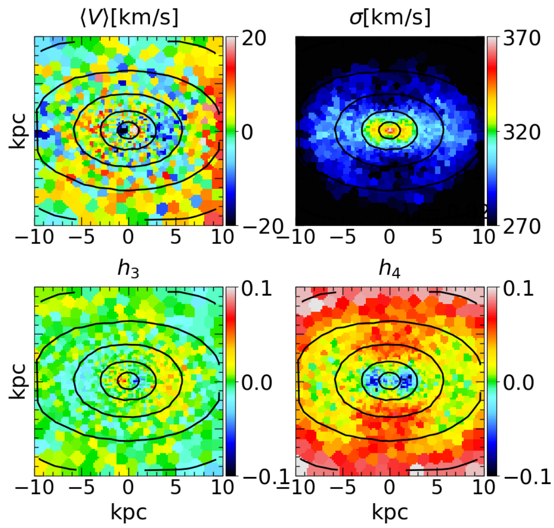

(b) BH-5 merger

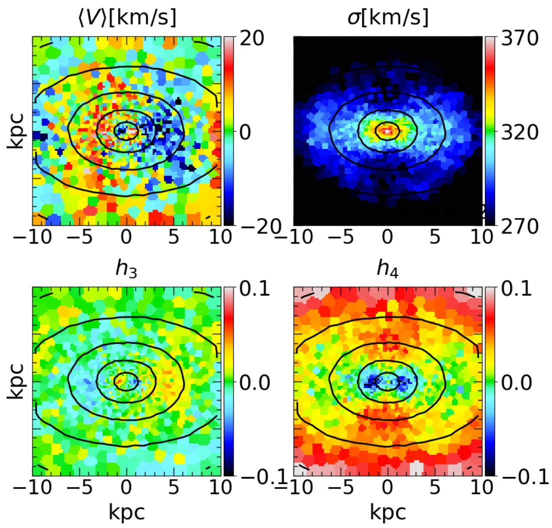

(c) BH-6 merger

Figure B.5: IFU-maps of average LOS-velocities, velocity dispersion, h_3 parameters and h_4 parameters from three simulated merger remnants: Snapshot-4, Snapshot-5 and Snapshot-6.

Bibliography

R. Bender, R. P. Saglia, and O. E. Gerhard. Line-of-sight velocity distributions of elliptical galaxies. *Monthly Notices of the Royal Astronomical Society*, 269: 785–813, Aug 1994. doi: 10.1093/mnras/269.3.785.

James Binney and Scott Tremaine. *Galactic Dynamics: Second Edition*. 2008.

M. Cappellari, E. Emsellem, D. Krajnović, R. M. McDermid, N. Scott, G. A. Verdoes Kleijn, L. M. Young, K. Alatalo, R. Bacon, L. Blitz, M. Bois, F. Bournaud, M. Bureau, R. L. Davies, T. A. Davis, P. T. de Zeeuw, P.-A. Duc, S. Khochfar, H. Kuntschner, P.-Y. Lablanche, R. Morganti, T. Naab, T. Oosterloo, M. Sarzi, P. Serra, and A.-M. Weijmans. The ATLAS^{3D} project - I. A volume-limited sample of 260 nearby early-type galaxies: science goals and selection criteria. *Monthly Notices of the Royal Astronomical Society*, 413:813–836, May 2011. doi: 10.1111/j.1365-2966.2010.18174.x.

Michele Cappellari. Structure and Kinematics of Early-Type Galaxies from Integral Field Spectroscopy. *Annual Review of Astronomy and Astrophysics*, 54:597–665, Sep 2016. doi: 10.1146/annurev-astro-082214-122432.

Michele Cappellari and Yannick Copin. Adaptive spatial binning of integral-field spectroscopic data using Voronoi tessellations. *Monthly Notices of the Royal Astronomical Society*, 342(2):345–354, Jun 2003. doi: 10.1046/j.1365-8711.2003.06541.x.

Michele Cappellari, Eric Emsellem, R. Bacon, M. Bureau, Roger L. Davies, P. T. de Zeeuw, Jesús Falcón-Barroso, Davor Krajnović, Harald Kuntschner, Richard M. McDermid, Reynier F. Peletier, Marc Sarzi, Remco C. E. van den Bosch, and Glenn van de Ven. The SAURON project - X. The orbital anisotropy of elliptical and lenticular galaxies: revisiting the (V/σ, $\in$) diagram with integral-field stellar kinematics. *Monthly Notices of the Royal Astronomical Society*, 379(2):418–444, Aug 2007. doi: 10.1111/j.1365-2966.2007.11963.x.

C. Marcella Carollo, Marijn Franx, Garth D. Illingworth, and Duncan A. Forbes. Ellipticals with Kinematically Distinct Cores: V - I Color Images with WPFC2. *The Astrophysical Journal*, 481(2):710–734, May 1997. doi: 10.1086/304060.

H. R. de Ruiter, P. Parma, A. Capetti, R. Fanti, R. Morganti, and L. Santantonio. Are radio galaxies and quiescent galaxies different? Results from the analysis of HST brightness profiles. *Astronomy and Astrophysics*, 439(2):487–496, Aug 2005. doi: 10.1051/0004-6361:20042529.

W. Dehnen. A Family of Potential-Density Pairs for Spherical Galaxies and Bulges. *Monthly Notices of the Royal Astronomical Society*, 265:250, Nov 1993. doi: 10.1093/mnras/265.1.250.

Bililign T. Dullo and Alister W. Graham. Sizing up Partially Depleted Galaxy Cores. *The Astrophysical Journal*, 755(2):163, August 2012. doi: 10.1088/0004-637X/755/2/163.

E. Emsellem, M. Cappellari, R. F. Peletier, R. M. McDermid, R. Bacon, M. Bureau, Y. Copin, R. L. Davies, D. Krajnović, H. Kuntschner, B. W. Miller, and P. T. de Zeeuw. The SAURON project - III. Integral-field absorption-line kinematics of 48 elliptical and lenticular galaxies. *Monthly Notices of the Royal Astronomical Society*, 352:721–743, August 2004. doi: 10.1111/j.1365-2966.2004.07948.x.

E. Emsellem, M. Cappellari, D. Krajnović, K. Alatalo, L. Blitz, M. Bois, F. Bournaud, M. Bureau, R. L. Davies, T. A. Davis, P. T. de Zeeuw, S. Khochfar, H. Kuntschner, P.-Y. Lablanche, R. M. McDermid, R. Morganti, T. Naab, T. Oosterloo, M. Sarzi, N. Scott, P. Serra, G. van de Ven, A.-M. Weijmans, and L. M. Young. The ATLAS^{3D} project - III. A census of the stellar angular momentum within the effective radius of early-type galaxies: unveiling the distribution of fast and slow rotators. *Monthly Notices of the Royal Astronomical Society*, 414:888–912, June 2011. doi: 10.1111/j.1365-2966.2011.18496.x.

Eric Emsellem, Michele Cappellari, Davor Krajnović, Glenn van de Ven, R. Bacon, M. Bureau, Roger L. Davies, P. T. de Zeeuw, Jesús Falcón-Barroso, Harald Kuntschner, Richard McDermid, Reynier F. Peletier, and Marc Sarzi. The SAURON project - IX. A kinematic classification for early-type galaxies. *Monthly Notices of the Royal Astronomical Society*, 379(2):401–417, Aug 2007. doi: 10.1111/j.1365-2966.2007.11752.x.

Laura Ferrarese and David Merritt. A Fundamental Relation between Supermassive Black Holes and Their Host Galaxies. *The Astrophysical Journal*, 539(1):L9–L12, Aug 2000. doi: 10.1086/312838.

O. E. Gerhard. Line-of-sight velocity profiles in spherical galaxies: breaking the degeneracy between anisotropy and mass. *Monthly Notices of the Royal Astronomical Society*, 265:213, Nov 1993. doi: 10.1093/mnras/265.1.213.

Ortwin Gerhard, Gunther Jeske, R. P. Saglia, and Ralf Bender. Breaking the degeneracy between anisotropy and mass: the dark halo of the E0 galaxy NGC6703. *Monthly Notices of the Royal Astronomical Society*, 295(1):197–215, Mar 1998. doi: 10.1046/j.1365-8711.1998.29511341.x.

Charles F. Goullaud, Joseph B. Jensen, John P. Blakeslee, Chung-Pei Ma, Jenny E. Greene, and Jens Thomas. The MASSIVE Survey. IX. Photometric Analysis of 35

High-mass Early-type Galaxies with HST WFC3/IR. *The Astrophysical Journal*, 856(1):11, March 2018. doi: 10.3847/1538-4357/aab1f3.

Alister W. Graham, Peter Erwin, I. Trujillo, and A. Asensio Ramos. A New Empirical Model for the Structural Analysis of Early-Type Galaxies, and A Critical Review of the Nuker Model. *The Astronomical Journal*, 125(6):2951–2963, Jun 2003a. doi: 10.1086/375320.

Alister W. Graham, Peter Erwin, I. Trujillo, and A. Asensio Ramos. A New Empirical Model for the Structural Analysis of Early-Type Galaxies, and A Critical Review of the Nuker Model. *The Astronomical Journal*, 125(6):2951–2963, Jun 2003b. doi: 10.1086/375320.

Davor Krajnović, Eric Emsellem, Michele Cappellari, Katherine Alatalo, Leo Blitz, Maxime Bois, Frédéric Bournaud, Martin Bureau, Roger L. Davies, Timothy A. Davis, P. T. de Zeeuw, Sadegh Khochfar, Harald Kuntschner, Pierre-Yves Lablanche, Richard M. McDermid, Raffaella Morganti, Thorsten Naab, Tom Oosterloo, Marc Sarzi, Nicholas Scott, Paolo Serra, Anne-Marie Weijmans, and Lisa M. Young. The ATLAS^{3D} project - II. Morphologies, kinemetric features and alignment between photometric and kinematic axes of early-type galaxies. *Monthly Notices of the Royal Astronomical Society*, 414(4):2923–2949, Jul 2011. doi: 10.1111/j.1365-2966.2011.18560.x.

T. R. Lauer, E. A. Ajhar, Y. I. Byun, A. Dressler, S. M. Faber, C. Grillmair, J. Kormendy, D. Richstone, and S. Tremaine. The Centers of Early-Type Galaxies with HST.I.An Observational Survey. *The Astronomical Journal*, 110:2622, Dec 1995. doi: 10.1086/117719.

Tod R. Lauer, S. M. Faber, Douglas Richstone, Karl Gebhardt, Scott Tremaine, Marc Postman, Alan Dressler, M. C. Aller, Alexei V. Filippenko, and Richard

Green. The Masses of Nuclear Black Holes in Luminous Elliptical Galaxies and Implications for the Space Density of the Most Massive Black Holes. *The Astrophysical Journal*, 662(2):808–834, Jun 2007a. doi: 10.1086/518223.

Tod R. Lauer, Karl Gebhardt, S. M. Faber, Douglas Richstone, Scott Tremaine, John Kormendy, M. C. Aller, Ralf Bender, Alan Dressler, and Alexei V. Filippenko. The Centers of Early-Type Galaxies with Hubble Space Telescope. VI. Bimodal Central Surface Brightness Profiles. *The Astrophysical Journal*, 664(1):226–256, July 2007b. doi: 10.1086/519229.

Matias Mannerkoski, Peter H. Johansson, Pauli Pihajoki, Antti Rantala, and Naab Thorsten. Inspiral of Supermassive Black Holes In Galactic Scale Simulations. *Monthly Notices of the Royal Astronomical Society*, 856(1):11, ? 2019. doi: 10.3847/1538-4357/aab1f3.

Miloš Milosavljević and David Merritt. Formation of Galactic Nuclei. *The Astrophysical Journal*, 563(1):34–62, Dec 2001. doi: 10.1086/323830.

Gerald D. Quinlan and Lars Hernquist. The dynamical evolution of massive black hole binaries — II. Self-consistent N-body integrations. *New Astronomy*, 2(6): 533–554, Dec 1997. doi: 10.1016/S1384-1076(97)00039-0.

Antti Rantala, Peter H. Johansson, Thorsten Naab, Jens Thomas, and Matteo Frigo. The Formation of Extremely Diffuse Galaxy Cores by Merging Supermassive Black Holes. *The Astrophysical Journal*, 864(2):113, September 2018. doi: 10.3847/1538-4357/aada47.

J. Thomas, R. P. Saglia, R. Bender, D. Thomas, K. Gebhardt, J. Magorrian, E. M. Corsini, and G. Wegner. Dynamical modelling of luminous and dark matter in 17 Coma early-type galaxies. *Monthly Notices of the Royal Astronomical Society*, 382(2):657–684, Dec 2007. doi: 10.1111/j.1365-2966.2007.12434.x.

J. Thomas, R. P. Saglia, R. Bender, P. Erwin, and M. Fabricius. The Dynamical Fingerprint of Core Scouring in Massive Elliptical Galaxies. *The Astrophysical Journal*, 782(1):39, Feb 2014. doi: 10.1088/0004-637X/782/1/39.

Jens Thomas, Chung-Pei Ma, Nicholas J. McConnell, Jenny E. Greene, John P. Blakeslee, and Ryan Janish. A 17-billion-solar-mass black hole in a group galaxy with a diffuse core. *Nature*, 532(7599):340–342, April 2016. doi: 10.1038/nature17197.

Roeland P. van der Marel and Marijn Franx. A New Method for the Identification of Non-Gaussian Line Profiles in Elliptical Galaxies. *The Astrophysical Journal*, 407:525, Apr 1993. doi: 10.1086/172534.

Melanie Veale, Chung-Pei Ma, Jens Thomas, Jenny E. Greene, Nicholas J. McConnell, Jonelle Walsh, Jennifer Ito, John P. Blakeslee, and Ryan Janish. The MASSIVE Survey - V. Spatially resolved stellar angular momentum, velocity dispersion, and higher moments of the 41 most massive local early-type galaxies. *Monthly Notices of the Royal Astronomical Society*, 464(1):356–384, January 2017. doi: 10.1093/mnras/stw2330.

Melanie Veale, Chung-Pei Ma, Jenny E. Greene, Jens Thomas, John P. Blakeslee, Jonelle L. Walsh, and Jennifer Ito. The MASSIVE survey - VIII. Stellar velocity dispersion profiles and environmental dependence of early-type galaxies. *Monthly Notices of the Royal Astronomical Society*, 473(4):5446–5467, February 2018. doi: 10.1093/mnras/stx2717.

Marcel Zemp, Oleg Y. Gnedin, Nickolay Y. Gnedin, and Andrey V. Kravtsov. On Determining the Shape of Matter Distributions. *The Astrophysical Journal Supplement*, 197(2):30, December 2011. doi: 10.1088/0067-0049/197/2/30.